Drag reduction capability of uniform blowing in supersonic wall-bounded turbulent flows

Yukinori Kametani,[1,*] Ayane Kotake,[2] Koji Fukagata,[2] and Naoko Tokugawa[3]
[1]*Institute of Industrial Science, University of Tokyo, 4-6-1 Komaba, Meguro-ku, Tokyo 153-8505, Japan*
[2]*Department of Mechanical Engineering, Keio University, Hiyoshi 3-14-1, Kohoku-ku, Yokohama 223-8522, Japan*
[3]*Aeronautical Technology Directorate, Japan Aerospace Exploration Agency, Osawa 6-13-11, Mitaka, Tokyo 181-0015, Japan*
(Received 28 June 2017; published 29 December 2017)

Drag reduction capability of uniform blowing in supersonic turbulent boundary layers is investigated by means of direct numerical simulation of channel flows with uniform blowing on one side and suction on the other. The bulk Reynolds number based on the bulk density, the bulk mean velocity, the channel half-width, and the viscosity on the wall is set to $\mathrm{Re}_b = 3000$. The bulk Mach number is set at 0.8 and 1.5 to investigate a subsonic and a supersonic condition, respectively. The amplitude of the blowing or suction is set to be 0.1%, 0.3%, or 0.5% of the bulk mass flow rate. At both Mach numbers, modifications of the mean streamwise velocity profiles with blowing and suction are found to be similar to those in an incompressible turbulent channel flow: The skin friction is reduced on the blowing side, while it is increased on the suction side. As for the drag reducing effect of blowing, the drag reduction rate and net-energy saving rate are hardly affected by the Mach number, while the control gain is increased with the increase of Mach number due to the increased density near the wall. The compressibility effect of drag reduction and enhancement is also examined using the physical decomposition of the skin friction drag. A noticeable Mach number effect is found only for the contribution terms containing the viscosity, which is increased by the increased temperature.

DOI: 10.1103/PhysRevFluids.2.123904

I. INTRODUCTION

In order to reduce skin friction drag in turbulent boundary layers, which is much higher than that in laminar flows due to near-wall turbulent structures [1], various techniques have been studied especially since Kim *et al.* [2] performed a direct numerical simulation (DNS) of an incompressible turbulent channel flow [3]. In addition to the passive control methods such as riblets [4] and superhydrophobic surfaces [5,6], active feedback (i.e., closed-loop) control methods have extensively been studied aiming at greater drag reduction effects [3,7,8]. As a classical example, Choi *et al.* [9] suggested the opposition control, in which the skin friction drag is reduced by about 20%–25% by applying local blowing and suction from the walls so as to oppose the quasistreamwise vortices.

In contrast to the closed-loop control, which requires high fabrication cost for tiny sensors and actuators [8], it has recently been demonstrated that predetermined approaches (i.e., open-loop control) also have a high potential for friction drag reduction. Min *et al.* [10] used an upstream traveling-wave-like blowing and suction from the walls in a turbulent channel flow and demonstrated that the drag could be reduced to a sublaminar level (although the total power required to drive the flow has been proven greater than that for the laminar flow [11,12]). Nakanishi *et al.* [13] considered a downstream traveling-wave-like wall deformation instead of blowing and suction. They demonstrated that the flow could be relaminarized, whereby the drag was reduced by about 70% at a

*yukkam@iis.u-tokyo.ac.jp

relatively low Reynolds number. Very recently, Mamori *et al.* [14] performed an extensive parametric study of streamwise traveling-wave-like blowing and suction and showed that the relaminarization could also be achieved by a downstream traveling-wave-like blowing and suction.

On the other hand, it has been well known that uniform blowing or suction from the wall decreases or increases the drag in a turbulent boundary layer. With uniform blowing, the mean velocity profile is pushed away from the wall, whereby the velocity gradient on the wall becomes milder. With uniform suction, on the contrary, the velocity gradient is steepened. The mean velocity profile in the presence of uniform blowing or suction is reasonably well scaled by the modified logarithmic law of the wall proposed by Stevenson [15]. More detailed modification of turbulent structure was studied by Sumitani and Kasagi [16] by means of DNS of a turbulent channel flow with blowing on one wall and suction on the other wall. They found that the turbulence is enhanced on the blowing side (where the friction drag is reduced) and suppressed on the suction side (where the drag is increased). This counterintuitive phenomenon was quantitatively explained by Fukagata *et al.* [17] using the mathematical relationship between the friction drag and the turbulent statistics, called the Fukagata-Iwamoto-Kasagi (FIK) identity: On the blowing side, for instance, the contribution of the mean wall-normal momentum that works to reduce the drag is greater than the increased contribution of the Reynolds shear stress. For a spatially developing turbulent boundary layer with a uniform blowing, Kametani and Fukagata [18] performed a DNS at a relatively low Reynolds number and found that a blowing at the amplitude of only 0.1% of the freestream velocity could reduce more than 10% of the drag. A similar drag reduction effect has also been confirmed at higher Reynolds numbers [19–21].

The studies mentioned above have been made for incompressible flows. In practical high-speed applications, such as aircrafts, the Mach number Ma is often greater than the value where the assumption of incompressible flow holds. If one considers applying such a friction drag reduction technique to a supersonic aircraft, such as the silent supersonic transport [22] being developed at Japan Aerospace Exploration Agency whose cruising Mach number is $\mathrm{Ma} = 1.5$, consideration of the compressibility effect is inevitable.

Supersonic turbulent boundary layers have also been studied by means of DNS [23–26]. Among others, Lagha *et al.* [26] systematically studied the effect of compressibility on turbulence statistics in the Mach-number range from 2.5 up to 20. They showed that the turbulence statistics in supersonic and hypersonic boundary layers are basically similar to those of incompressible boundary layers and that a small difference is attributed to the variable density. A similar conclusion was obtained by the study of Gomez *et al.* [27], who extended the FIK identity [17] to compressible flows and quantitatively analyzed the different contributions to the friction drag in a supersonic turbulent boundary layer. They concluded that, similarly to incompressible flows, the dominant contributor to the skin friction is the Reynolds shear stress and the small difference from the incompressible flow comes from the variable dynamic viscosity. These findings imply that the effects of uniform blowing or suction through the wall in supersonic turbulent flows should also be similar to those in incompressible flows. However, this implication still needs to be confirmed on a solid basis.

In the present study, we perform direct numerical simulations of compressible turbulent channel flows with uniform blowing on one side and suction on the other side in order to investigate the similarity and difference in the control effects among an incompressible, a subsonic, and a supersonic condition. Similarly to the previous study on an incompressible channel flow [17], we investigate the compressibility effect on the skin friction modification using the physical decomposition using the compressible flow version of the FIK identity [27]. We also discuss the control efficiency in terms of the net-energy saving rate and the gain.

II. DIRECT NUMERICAL SIMULATION

We consider a flow between two parallel walls kept at the same temperature θ_w^* (hereafter, the subscript w denotes quantities on the wall). The governing equations are the continuity, the

Navier-Stokes, and the energy transport equations for a compressible flow, i.e.,

$$\frac{\partial \rho}{\partial t} = -\frac{\partial \rho u_i}{\partial x_i}, \tag{1}$$

$$\frac{\partial \rho u_i}{\partial t} = -\frac{\partial \rho u_i u_j}{\partial x_j} - \frac{\partial p}{\partial x_i} + \frac{1}{\mathrm{Re}}\frac{\partial \tau_{ij}}{\partial x_j} + f_b \delta_{i1}, \tag{2}$$

$$\frac{\partial \rho \theta}{\partial t} = -\frac{\partial \rho \theta u_j}{\partial x_j} - (\gamma - 1)\rho\theta\frac{\partial u_j}{\partial x_j} - \frac{\gamma}{\mathrm{Re}\,\mathrm{Pr}}\frac{\partial q_j}{\partial x_j} + \frac{\gamma(\gamma-1)\mathrm{Ma}}{Re}\tau_{ij}\frac{\partial u_i}{\partial x_j}. \tag{3}$$

The density ρ, the velocity components u_i, the coordinates x_i, and the time t are made dimensionless by the bulk density ρ_b^*, the bulk velocity U_b^*, and the channel half-width δ^*, where the asterisk denotes dimensional quantities. The Einstein summation convention applies to the dummy indices. For convenience, the velocity components u_1, u_2, and u_3 are also denoted by u, v, and w, respectively. The bulk density ρ_b^* and the bulk mean velocity U_b^* are defined as

$$\rho_b^* = \frac{1}{2\delta^*}\int_0^{2\delta^*} \langle \rho^* \rangle dy^* \tag{4}$$

and

$$U_b^* = \frac{1}{2\delta^* \rho_b^*}\int_0^{2\delta^*} \langle \rho^* u^* \rangle dy^*, \tag{5}$$

where $\langle \cdot \rangle$ denotes the Reynolds average. Following the DNS of Coleman *et al.* [23], the bulk Reynolds number is defined as $\mathrm{Re} = \rho_b^* U_b^* / \mu_w^*$, where μ_w^* is the dynamic viscosity on the wall. The temperature θ is made dimensionless by the wall temperature of the isothermal wall θ_w^*. The Prandtl number and the bulk Mach number are defined as $\mathrm{Pr} = \mu_w^* c_p^* / \lambda_w^*$ and $\mathrm{Ma} = U_b^*/c^*$, where c_p^*, λ_w^*, and c^* are the specific heat under constant pressure, the thermal conductivity on the wall, and the speed of sound, respectively; γ is the specific heat ratio ($\gamma = 1.4$ in the present study).

The viscous stress τ_{ij} and the heat flux q_i are calculated by

$$\tau_{ij} = \mu\left(\frac{\partial u_i}{\partial x_j} + \frac{\partial u_j}{\partial x_i} - \frac{2}{3}\delta_{ij}\frac{\partial u_l}{\partial x_l}\right) \tag{6}$$

and

$$q_i = -\lambda\frac{\partial \theta}{\partial x_i}, \tag{7}$$

where δ_{ij} denotes the Kronecker delta and the Stokes hypothesis has been assumed. Similarly to Coleman *et al.* [23], the dimensionless viscosity μ and the dimensionless thermal conductivity λ are calculated by assuming the power law, i.e.,

$$\mu = \lambda = \theta^{0.7}, \tag{8}$$

and the thermodynamical variables ρ, θ, and p are related to one another by the perfect gas state equation, i.e.,

$$\gamma\,\mathrm{Ma} p = \rho\theta. \tag{9}$$

The periodic boundary condition is used in the streamwise and spanwise directions. The no-slip condition is applied on the walls, i.e., $(\rho u_i)_w = 0$. In the cases with uniform blowing and suction, a constant wall-normal mass flow is added to the wall boundary condition, i.e., $\dot{m}_w = (\rho v)_w = \mathrm{const}$ (>0), on both walls, as shown in Fig. 1.

The bulk Mach number is set at $\mathrm{Ma} = 0.8$ and 1.5 (hereafter referred to as the Ma0.8 and Ma1.5 cases, respectively). The bulk mass flux $\dot{m}_b = (\rho U)_b$ is kept constant by adjusting the effective pressure gradient f_b so that the bulk Reynolds numbers is fixed at $\mathrm{Re} = 3000$. The magnitude of

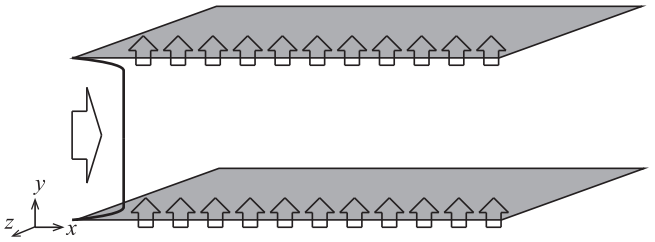

FIG. 1. Schematic of the computational domain.

mass flux through the walls is varied as $\dot{m}_w = 0.001$, 0.003, and 0.005, i.e., 0.1%, 0.3%, and 0.5% of the bulk mass flow rate.

The present DNS code for a compressible flow was developed based on that for an incompressible channel flow of Fukagata *et al.* [28]. The governing equations are discretized by the fourth-order fully conservative central-finite-difference method of Morinishi *et al.* [29] for the advection term in the streamwise and the spanwise direction, while the second-order fully conservative central-finite-difference method is used for the wall-normal direction. The second-order central-finite-difference method is used for the other terms. The time integration is done by using the low-storage third-order Runge-Kutta–Crank-Nicolson (RK3-CN) scheme [30]. For comparison with an incompressible case, we also performed simulations using the incompressible DNS code of Fukagata *et al.* [28], in which the energy-conservative second-order finite-difference method [31] is used for the spatial discretization and the RK3-CN scheme is used for the time integration together with the simplified marker and cell [32] –like velocity-pressure coupling.

The streamwise, the wall-normal, and the spanwise lengths of the computational domain are $(L_x, L_y, L_z) = (4\pi\delta, 2\delta, 4\pi\delta/3)$. The corresponding numbers of grid points are $(N_x, N_y, N_z) = (256, 120, 128)$ and the resultant grid resolutions are $(\Delta x^{+0}, \Delta y^{+0}_{\min}, \Delta z^{+0}) = (9.32, 0.22, 6.22)$ in the Ma0.8 case and (10.8, 0.26, 7.80) in the Ma1.5 case, where the superscript $+0$ denotes the wall units in the base flow (i.e., without blowing and suction). The grid is uniform in the streamwise and spanwise directions and stretched in the wall-normal direction using a hyperbolic tangent function.

III. BASE FLOW

First, the results for the cases without blowing and suction are presented. The physical and computational conditions used are listed in Table I. In order to validate the present compressible flow code, the major statistics are compared with literature. The statistics are accumulated in the period of $T^{+0} \approx 3000$. First of all, the resultant friction Reynolds number Re_τ in the Ma1.5 case is found to be in good agreement with those of Coleman *et al.* [23] and Morinishi *et al.* [24].

Hereafter, $\langle\cdot\rangle$ denote the Reynolds average whereas $\{\cdot\}$ denotes the Favre average, i.e., $\{f\} = \langle\rho f\rangle/\langle\rho\rangle$. The fluctuations with respect to these averages are defined, respectively, as $f' = f - \langle f\rangle$ and $f'' = f - \{f\}$.

TABLE I. Conditions used for base flow and the resultant friction Reynolds number Re_τ.

Case	Re_τ	Ma	Pr	γ	$L_x \times L_y \times L_z$	$N_x \times N_y \times N_z$
Ma0.0	188	incompressible			$4\pi\delta \times 2\delta \times 4\pi\delta/3$	$256 \times 120 \times 128$
Ma0.8	190	0.8	0.72	1.4	$4\pi\delta \times 2\delta \times 4\pi\delta/3$	$256 \times 120 \times 128$
Ma1.5	220	1.5	0.72	1.4	$4\pi\delta \times 2\delta \times 4\pi\delta/3$	$256 \times 120 \times 128$
Coleman *et al.* [23]	222	1.5	0.7	1.4	$4\pi\delta \times 2\delta \times 4\pi\delta/3$	$144 \times 119 \times 80$
Morinishi *et al.* [24]	218	1.5	0.72	1.4	$4\pi\delta \times 2\delta \times 4\pi\delta/3$	$120 \times 180 \times 120$

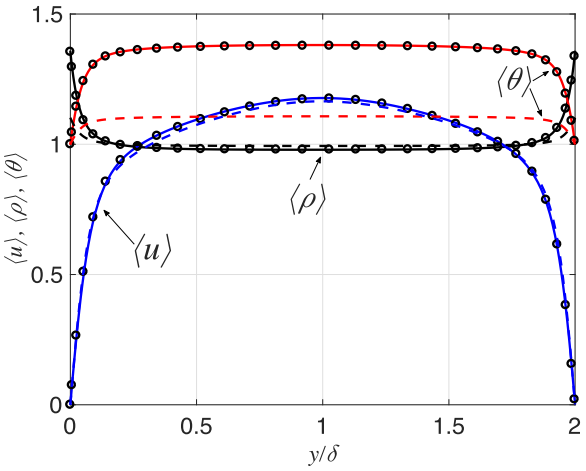

FIG. 2. Mean streamwise velocity $\langle u\rangle$ (blue), mean density $\langle\rho\rangle$ (black), and mean temperature $\langle\theta\rangle$ (red). The solid line shows Ma = 1.5, the dashed line shows Ma = 0.8, and circles show the Ma = 1.5 case of Coleman *et al.* [23].

The Reynolds-averaged streamwise velocity $U = \langle u\rangle$, density $\langle\rho\rangle$, and temperature $\langle\theta\rangle$ are plotted in Fig. 2. The temperature is increased in the bulk of the channel and the density is increased in the vicinity of the walls. The profiles are found to be in good agreement with the results of Coleman *et al.* [23] at Ma = 1.5.

The Reynolds-averaged temperature at the center of the channel $\langle\theta_c\rangle$ and the density on the wall $\langle\rho_w\rangle$, and the density at the center of the channel $\langle\rho_c\rangle$ are listed in Table II. Again, the values at Ma = 1.5 are in good agreement with those of Coleman *et al.* [23]. The table also shows that a lower Mach number results in lower values of $\langle\theta_c\rangle$ and $\langle\rho_c\rangle$.

Figure 3 shows the profiles of the van Driest–transformed mean streamwise velocity, i.e.,

$$U_{\mathrm{vD}} = \int_0^{\langle u\rangle} \left(\frac{\langle\rho\rangle}{\langle\rho\rangle_w}\right)^{1/2} d\langle u\rangle, \tag{10}$$

in wall units, which also collapses with that of Coleman *et al.* [23]. It is also noticed that the velocity in the logarithmic-law region is slightly higher in the supersonic case (Ma = 1.5) than that in the subsonic case (Ma = 0.8).

The root-mean-square (rms) values of the streamwise, the wall-normal, and the spanwise velocity fluctuations, i.e., u_{rms} v_{rms}, and w_{rms}, are plotted in Fig. 4. As the Mach number increases, the rms values increase due to the increase of density near the wall [26]. At Ma = 1.5, the rms velocity fluctuations are in good agreement with those of Coleman *et al.* [23].

TABLE II. Temperature and density on the wall and at the center of the channel.

Case	Ma	$\langle\theta_c\rangle$	$\langle\rho_w\rangle$	$\langle\rho_c\rangle$
Ma0.8	0.8	1.11	1.10	0.99
Ma1.5	1.5	1.38	1.37	0.98
Coleman *et al.* [23]	1.5	1.38	1.36	0.98

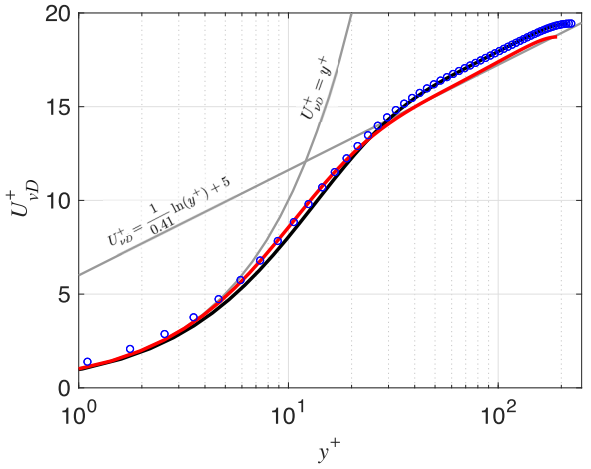

FIG. 3. The van Driest–transformed mean streamwise velocity. The black line shows Ma = 1.5, the red line shows Ma = 0.8, and blue circles show Ma = 1.5 of Coleman *et al.* [23].

Figure 5 shows the shear stress balance based on the approximated momentum equation [33]

$$\underbrace{\langle\mu\rangle\frac{\partial\{u^+\}}{\partial y^+}}_{\mathrm{I}} + \underbrace{\langle\mu\rangle\frac{\partial\langle u''^+\rangle}{\partial y^+}}_{\mathrm{II}} + \underbrace{\left\langle\mu'\frac{\partial u'^+}{\partial y^+}\right\rangle}_{\mathrm{III}} \underbrace{-\frac{\langle\rho\rangle}{\langle\rho_w\rangle}\{u''^+v''^+\}}_{\mathrm{IV}} = \underbrace{1 - \int_0^y \langle\rho\rangle dy}_{\mathrm{V}}. \tag{11}$$

It can be observed that the dominant contributors are the viscous shear stress (I) and the Reynolds shear stress (IV), while contributions from the other terms (II, III, and V) are very small. The total shear stress slightly deviates from the linear line due to the density variations, as reported by Huang *et al.* [33].

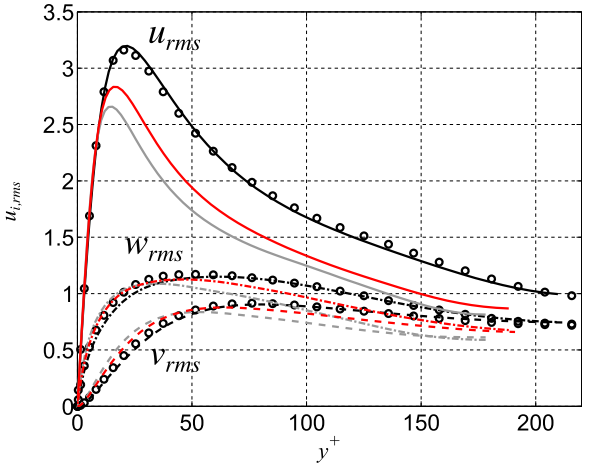

FIG. 4. Turbulent intensities. The black solid line shows Ma = 1.5, the red solid line Ma = 0.8, and the gray solid line the incompressible case. The solid lines are for u_{rms}, the dashed lines v_{rms}, and the dash-dotted lines w_{rms}. Circles mark Ma = 1.5 of Coleman *et al.* [23].

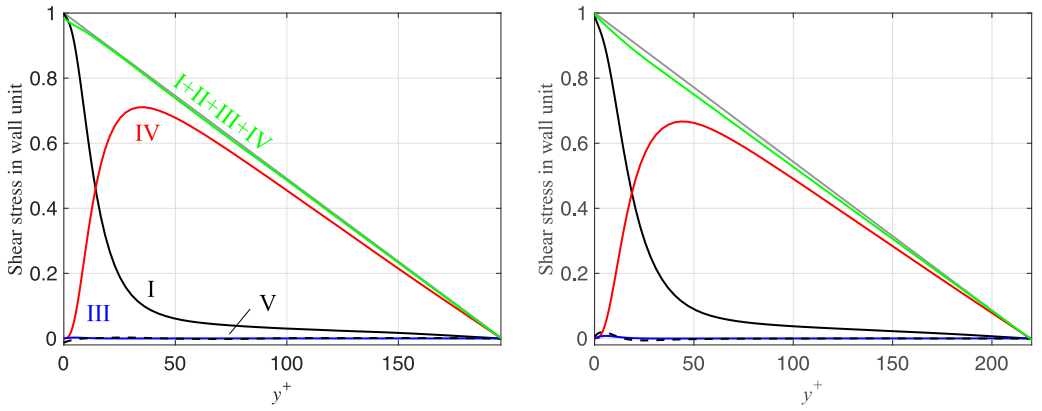

FIG. 5. Shear stress balance for Ma = 0.8 (left) and Ma = 1.5 (right). The black solid line shows term I in Eq. (11), the dashed black line term II the blue solid line term III, the red solid line term IV, and the green solid line I + II + III + IV.

IV. UNIFORM BLOWING AND SUCTION

A. Thermal properties

The turbulent statistics in the cases with uniform blowing and suction are presented here. The statistics are accumulated in the period of $T = 100\delta/U_b$ after the flow has reached its new statistically steady state, which corresponds to $T^{+0} \approx 1200$ in the Ma0.0 and Ma0.8 cases and $T^{+0} \approx 1600$ in the Ma1.5 case.

Profiles of the Reynolds-averaged density $\langle\rho\rangle$ and temperature $\langle\theta\rangle$ are depicted in Fig. 6. In both the subsonic and supersonic cases, the density profiles are observed to shift from the blowing side to the suction side. Although the density gradient is moderated on the blowing side and increased on the suction side, the minimum density around the center of the channel is hardly affected by the blowing and suction. This observation is also supported by the values of $\langle\rho_c\rangle$ presented in Table II and $\langle\rho\rangle_{\min}$ and $\langle\rho\rangle_{\max}$ presented in Table III. The Reynolds-averaged density on the wall in the subsonic case, listed in Table III, does not show a significant difference between the blowing side and the suction side. In the supersonic case, however, a small amount of increase and decrease in the

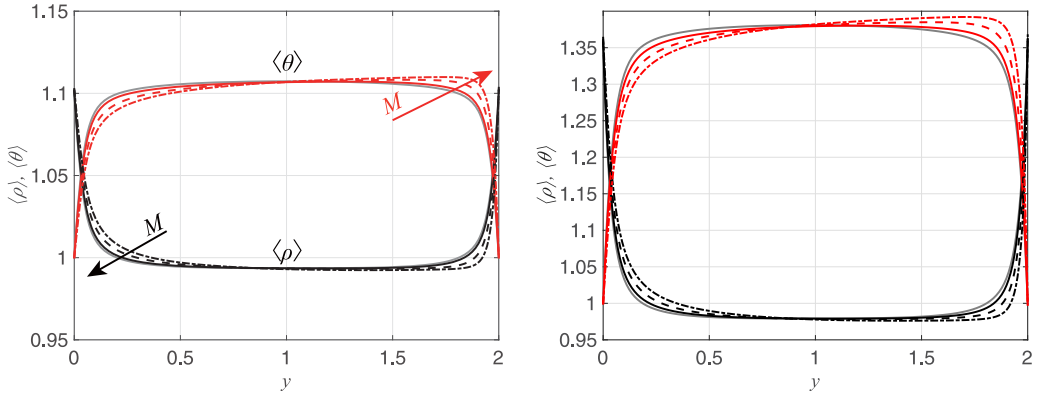

FIG. 6. Mean density (black) and temperature (red) profiles for Ma = 0.8 (left) and Ma = 1.5 (right). The solid line shows 0.1%, the dashed line 0.3%, the dash-dotted line 0.5%, and the gray solid line the uncontrolled case.

TABLE III. Thermodynamical properties.

Case	$\langle\rho_w^b\rangle$	$\langle\rho_w^s\rangle$	$\langle\rho\rangle_{\min}$	$\langle\theta\rangle_{\max}$
Ma0.8BS0.1	1.10	1.10	0.99	1.11
Ma0.8BS0.3	1.10	1.10	0.99	1.11
Ma0.8BS0.5	1.10	1.10	0.99	1.11
Ma1.5BS0.1	1.36	1.33	0.98	1.38
Ma1.5BS0.3	1.36	1.33	0.98	1.39
Ma1.5BS0.5	1.36	1.33	0.98	1.39

density is found on the blowing and suction sides, respectively. Table III also shows the maximum temperature $\langle\theta\rangle_{\max}$ around the center of the channel. In the subsonic case, the maximum temperature is hardly affected by blowing and suction. On the other hand, in the supersonic case, a slight increase of $\langle\theta\rangle_{\max}$ is found due to heating by viscous dissipation.

The density distribution in a y-z cross section is visualized in Fig. 7 together with the velocity vectors. The high-density region is thickened on the blowing side, while it is thinned on the suction side in both the Ma0.8BS0.5 and Ma1.5BS0.5 cases. Hereafter, the number following "BS" denotes the amplitude of blowing and suction (in percentage) to the bulk mean velocity; for instance, Ma0.8BS0.5 denotes the case of Ma $= 0.8$ and $\dot{m}_w = 5.0 \times 10^{-3}$. The higher bulk Mach number results in the higher density near the wall. It can also be observed that the density is entrained by the quasistreamwise vortices near the wall. Figure 7 also illustrates that the mass flux at a constant temperature introduced from the walls attenuates the density fluctuations on the isothermal walls. Similarly, the temperature decreases on the blowing side, while it increases on the suction side. While the maximum temperature $\langle\theta\rangle_{\max}$ in the subsonic cases is not affected by the blowing and suction, $\langle\theta\rangle_{\max}$ in the supersonic case is slightly increased due to enhanced turbulence when the blowing and suction amplitude is larger than 0.1%.

B. Turbulence statistics

The variation of density might directly affect on the Favre-averaged turbulence statistics. Figure 8 shows the van Driest–transformed mean streamwise velocity scaled by the local wall unit on each

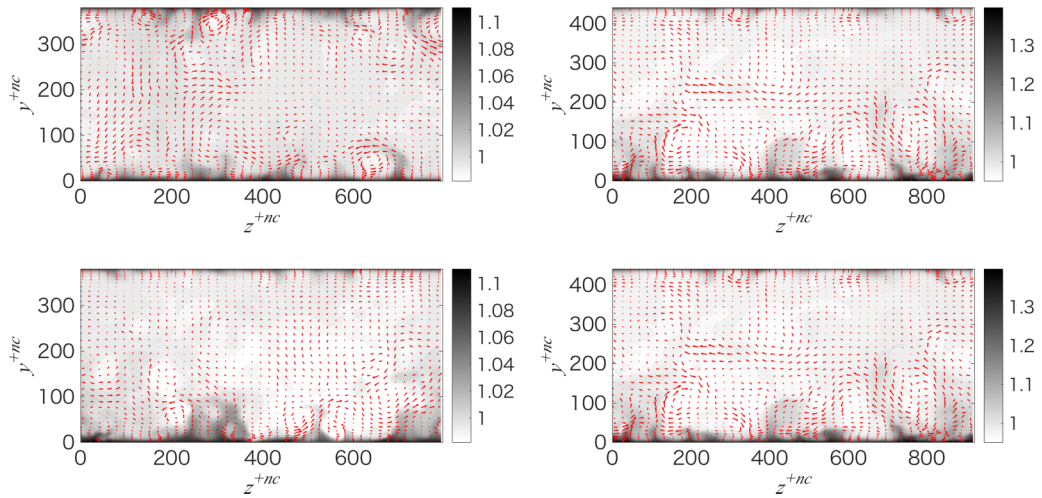

FIG. 7. Density distribution in the cross section: top left, Ma0.8; bottom left, Ma0.8BS0.5; top right, Ma1.5; and bottom right, Ma1.5BS0.5.

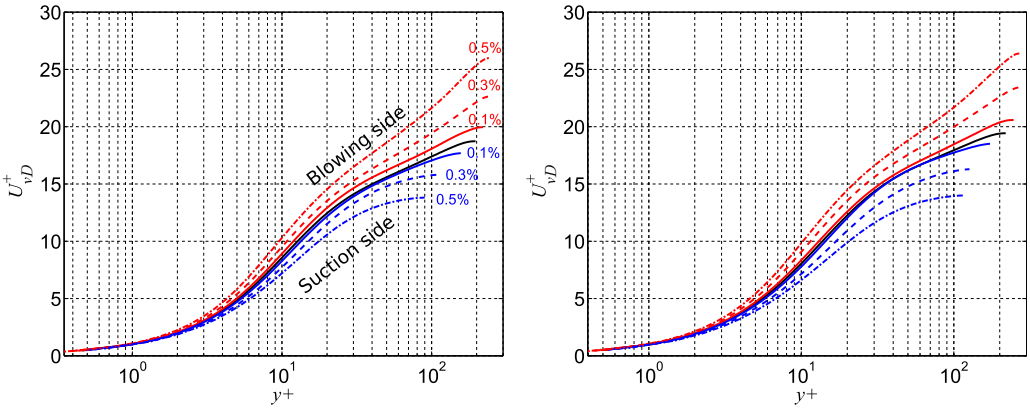

FIG. 8. The van Driest–transformed mean streamwise velocity for Ma = 0.8 (left) and Ma = 1.5 (right) for the uncontrolled case (black), the blowing side (red), and the suction side (blue). The solid lines show 0.1%, the dashed lines 0.3%, and the dash-dotted lines 0.5%.

wall. In both the Ma = 0.8 and Ma = 1.5 cases, the linear-law region can be found in the range of $y^+ < 2$. However, the logarithmic law does not seem appropriate anymore. An upward (downward) shift is observed in the blowing (suction) side due to the decreased (increased) friction velocity. The amount of such a shift becomes larger as the amplitude of blowing (suction) is increased.

The rms of velocity fluctuations in the local wall unit are plotted in Figs. 9 and 10. These figures show that all the components increase by blowing but decrease by suction under both the supersonic and subsonic conditions. Although the peak values cannot be scaled by the wall units, the peak location of the streamwise fluctuation is fixed at $y^+ \approx 15$, whether on the blowing side or the suction side and under the supersonic or subsonic conditions. A similar argument can be made about the wall-normal and spanwise fluctuations, i.e., $y^+ \approx 60$ for the wall-normal components and $y^+ \approx 40$ for the spanwise components.

In order to compare the shear stress distributions between the controlled case and the uncontrolled case, the viscous shear stress (VSS), i.e., term I in Eq. (11), and the Reynolds shear stress (RSS), i.e., term IV in Eq. (11), scaled by the wall units in the uncontrolled case are plotted in Fig. 11. It is apparent that, at both Ma = 0.8 and 1.5, RSS is increased on the blowing side, while it is decreased

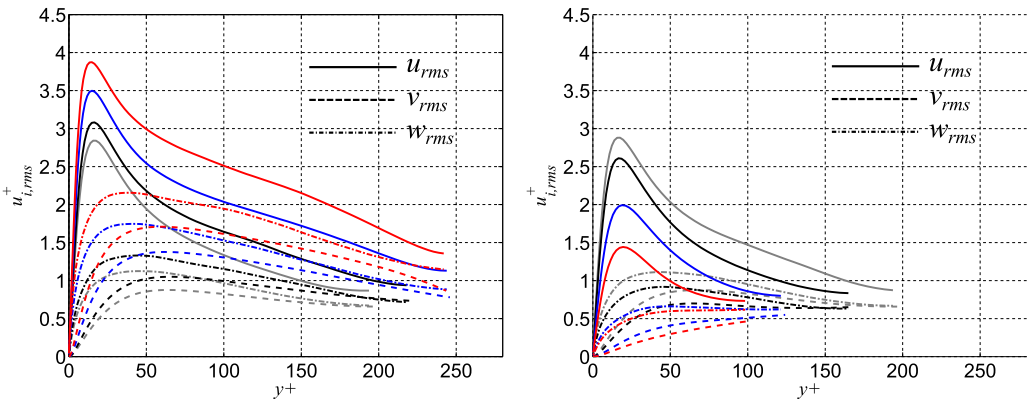

FIG. 9. Favre-averaged turbulent intensity at Ma = 0.8 for the blowing side (left) and the suction side (right). The solid lines show u', the dashed lines v', and the dash-dotted lines w'. Gray shows the uncontrolled case, black 0.1%, blue 0.3%, and red 0.5%.

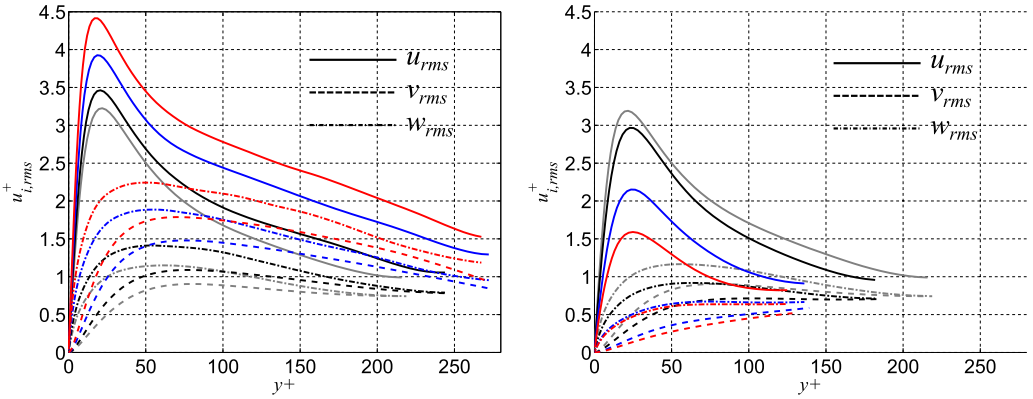

FIG. 10. Favre-averaged turbulent intensity at Ma = 1.5 for the blowing side (left) and the suction side (right). The solid lines show u', the dashed lines v', and the dash-dotted lines w'. Gray shows the uncontrolled case, black 0.1%, blue 0.3%, and red 0.5%.

on the suction side. On the other hand, VSS has the opposite trend: VSS is decreased on the blowing side and increased on the suction side. As a result, the summation of the two shear stresses (RSS + VSS) shifts towards the suction wall by uniform blowing and suction. The profiles of the total shear stress in the controlled case are not symmetric around the center of the channel; the wall-normal position of zero shear stress shifts towards the suction wall. Although the friction Reynolds number is different in the cases of Ma = 0.8 and 1.5, the amount of shift in the total shear stress looks to be determined primarily by the amplitude of blowing and suction rather than the Mach number. Here the vortical structures in the 0.5% blowing and suction case are visualized in Fig. 12 by the Laplacian of pressure. The number of vortices is decreased on the suction side, while it is increased on the blowing side, in accord with the modification in the Reynolds shear stress observed in Fig. 11. This trend is similar to that in the incompressible turbulent boundary layer [18–21].

C. Local Mach number

Although the Mach number based on the bulk velocity is fixed in each case, the local Mach number may be affected by the blowing or suction. Figure 13 shows the local Mach number

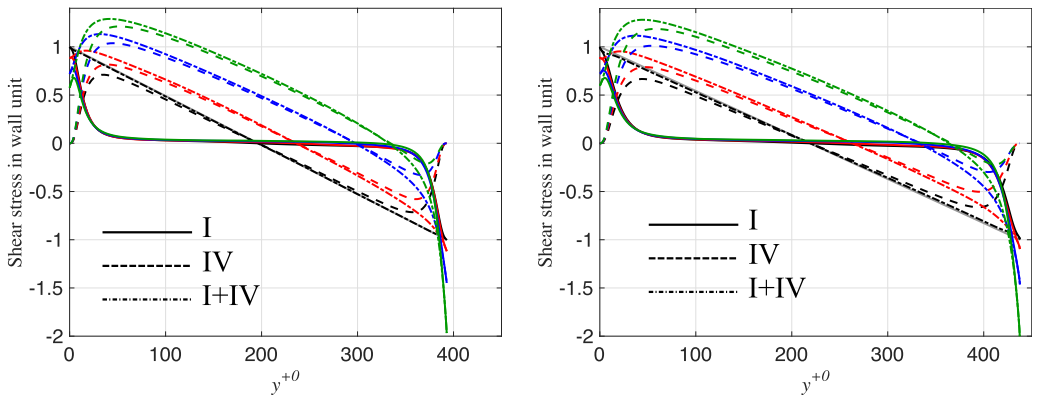

FIG. 11. Shear stress balance with blowing and suction for Ma = 0.8 (left) and Ma = 1.5 (right) for the uncontrolled case (black), 0.1% (red) 0.3% (blue), and 0.5% (green). Solid lines show term I in Eq. (11), dashed lines term IV, and dash-dotted lines term I + IV.

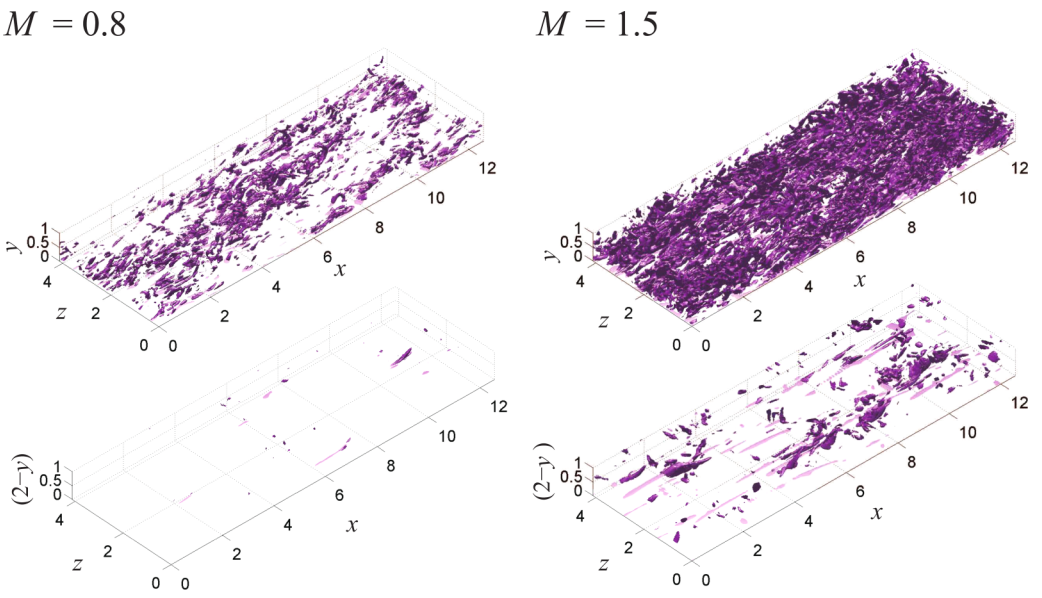

FIG. 12. Flow structures by isosurfaces of $\nabla^2 p = -2$ and contour of wall shear stress for the blowing side (top) and the suction side (bottom).

$\mathrm{Ma}_l = \mathrm{Ma}\langle u\rangle/\sqrt{\langle\theta\rangle}$ in both bulk-Mach-number cases. For the uncontrolled case and the 0.5% blowing and suction cases, the turbulent Mach number $\mathrm{Ma}_t = \mathrm{Ma}\sqrt{\langle u'^2 + v'^2 + w'^2\rangle}/\sqrt{\langle\theta\rangle}$ is also displayed as bands, i.e., $\mathrm{Ma}_l \pm \mathrm{Ma}_t$. The local Mach number is found to be below unity in the region near the walls in both Mach-number cases; namely, the flows are subsonic near the wall. The profiles show that in both cases the local Mach number is decreased on the blowing side, while it is increased on the suction side. This trend appears more strongly as the control amplitude increases. The rms of turbulent Mach number is increased on the blowing side, while it is decreased on the suction side.

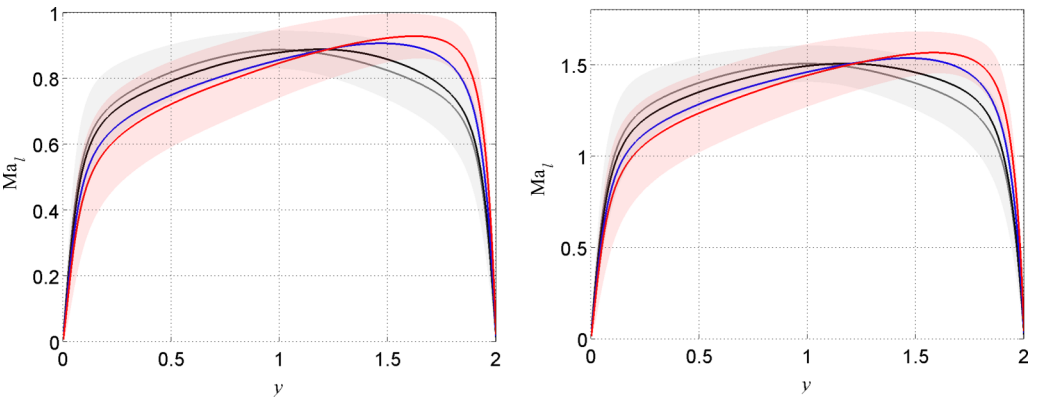

FIG. 13. Local Mach number as a function of y: Ma = 0.8 (left) and Ma = 1.5 (right) for the uncontrolled case (gray), 0.1%BS (black), 0.3% (blue), and 0.5% (red). Gray and red bands show the range of $\pm\mathrm{Ma}_t$ of the uncontrolled and 0.5%BS cases, respectively.

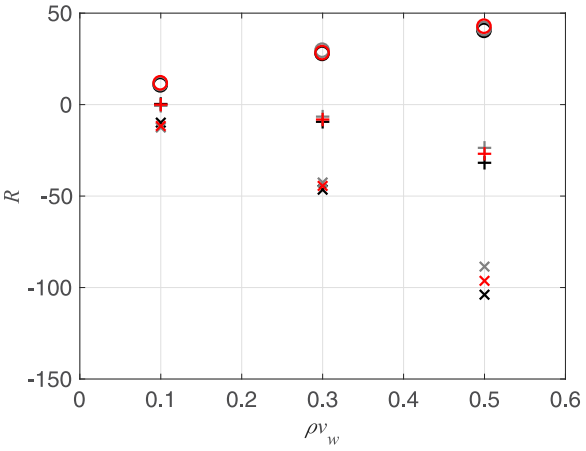

FIG. 14. Drag reduction rate R ($\times 10^2$) for Ma = 1.5 (black) and Ma = 0.8 (red) on the suction side, $\times$; the blowing side, $\circ$; and averaged, $+$.

D. Skin friction drag and heat transfer

Uniform blowing and suction affect the skin friction drag and the heat transfer. The drag reduction rate on the suction side, the blowing side, and their average are defined as

$$R^s = \frac{C_f^0 - C_f^s}{C_f^0}, \tag{12}$$

$$R^b = \frac{C_f^0 - C_f^b}{C_f^0}, \tag{13}$$

$$R = \frac{C_f^0 - \left(C_f^s + C_f^b\right)/2}{C_f^0}, \tag{14}$$

where the superscripts of s and b denote the suction side and the blowing side, respectively, and the friction coefficient C_f is defined as

$$C_f = \frac{2\tau_w^*}{\rho_w^* U_b^{*2}}. \tag{15}$$

Negative values of R indicate drag increase. The reduction rate in each case is shown in Fig. 14. The drag reduction (increase) rate on the blowing (suction) wall increases as the control amplitude increases. Although the drag reduction rate by blowing is nearly insensitive to the Mach number, the drag increase rate on the suction side is slightly increased with the Mach number.

Similarly, the heat transfer reduction rate can be defined

$$R_\theta^s = \frac{\mathrm{St}^0 - \mathrm{St}^s}{\mathrm{St}^0}, \tag{16}$$

$$R_\theta^b = \frac{\mathrm{St}^0 - \mathrm{St}^b}{\mathrm{St}^0}, \tag{17}$$

where the Stanton number St is defined as

$$\mathrm{St} = \frac{q_w^*}{c_p \theta_w^* U_b^*}. \tag{18}$$

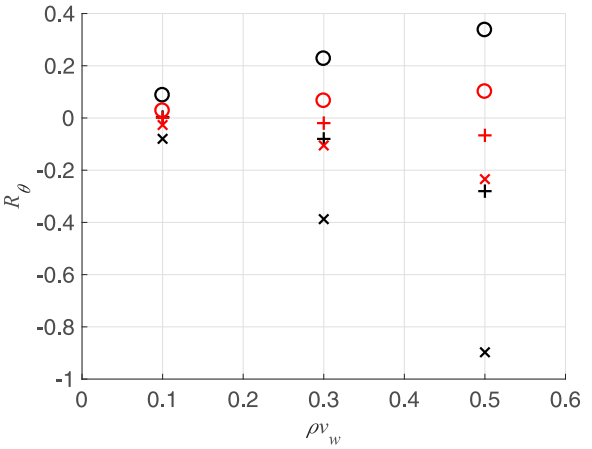

FIG. 15. Heat transfer reduction rate R_θ ($\times 10^2$) for Ma = 1.5 (black) and Ma = 0.8 (red) on the suction side, $\times$; the blowing side, $\circ$; and averaged, $+$.

The heat transfer reduction rate is plotted in Fig. 15. Although the Mach-number dependence of the heat transfer cannot directly be compared among different cases because the temperature profile varies with the Mach number, it is clear that the heat transfer is enhanced on the blowing side, while it is suppressed on the suction side. The average values show that the heat transfer is promoted in all controlled cases. The plot shows that the heat transfer is more sensitive to the amplitude of blowing and suction as well as the bulk Mach number. By blowing the cold fluid ($\theta = 1$) from the wall, the temperature gap between the near-wall region and the wall becomes smaller. By suction, in contrast, the temperature gap becomes larger since the hot fluid is attracted from the channel center towards the wall. This trend is more noticeable in the case of higher amplitude of blowing and suction, and this additional mechanism amplifies the effect of blowing and suction on heat transfer as compared to that on momentum.

The control efficiency on the blowing side is of great interest if we consider a boundary layer in practical applications, although the present simulation of channel flow includes the effect of suction on the opposite wall to keep the mass flux constant. The net-energy saving rate S and the control gain G on the blowing side are therefore defined as

$$S = \frac{C_f^0 - \left(C_f^b + W_{\text{in}}/U_b\right)}{C_f^0}, \tag{19}$$

$$G = \frac{C_f^0 - C_f^b}{W_{\text{in}}/U_b}, \tag{20}$$

where W_{in} is the input power of blowing defined as

$$W_{\text{in}} = \left\langle \tfrac{1}{2}\rho v^3 \right\rangle_w = \left\langle \tfrac{1}{2}\dot{m}_w v_w^2 \right\rangle \approx \tfrac{1}{2}\langle \rho_w \rangle \langle v_w \rangle^3. \tag{21}$$

Here, in order to discuss an ideal situation, the contribution from the pressure difference between the inside and outside of the blowing plate is assumed to be negligibly small compared to the one from the wall-normal velocity. The net-energy saving rate and the control gain is plotted in Fig. 16 as an S-G map. The figure shows that weaker amplitude of blowing results in higher control gain and lower net-energy saving rate, while higher amplitude of blowing works opposite at all bulk Mach numbers. Remarkably, the Mach-number dependence can be found: The control gain is increased as the bulk Mach number increases.

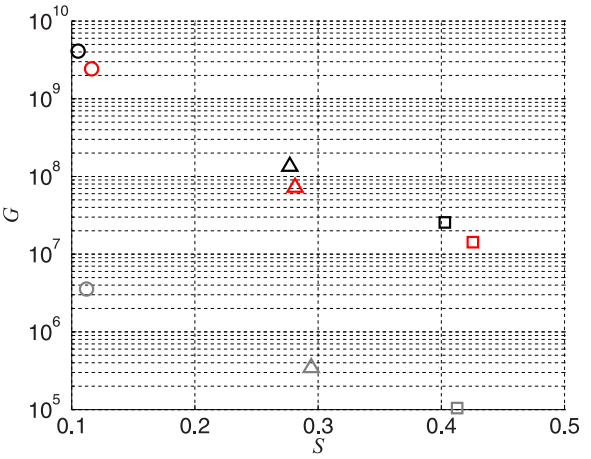

FIG. 16. The S-G map: gray, the incompressible case; black, Ma = 1.5; and red, Ma = 0.8 for 0.1%, ○; 0.3%, △; and 0.5%, □.

In order to investigate the reason for this Mach-number dependence, we take a look at the profile of the mean wall-normal velocity. Basically, the wall-normal velocity due to the mass flux introduced from the wall moves the mean streamwise velocity profile away from the wall. Although the mass flux works directly on the wall-normal velocity in the incompressible flow, that in the compressible flow works differently due to the variable density.

Figure 17 shows the Favre-averaged and the Reynolds-averaged wall-normal velocities. As the Mach number increases, the mean wall-normal velocity near the wall decreases. It is obvious that the Favre-averaged and the Reynolds-averaged wall-normal velocities do not agree with each other. On the blowing side, a clear gap between Favre-averaged and Reynolds-averaged profiles can be found. From the definition of the Favre-averaged and the Reynolds-averaged values, this gap is

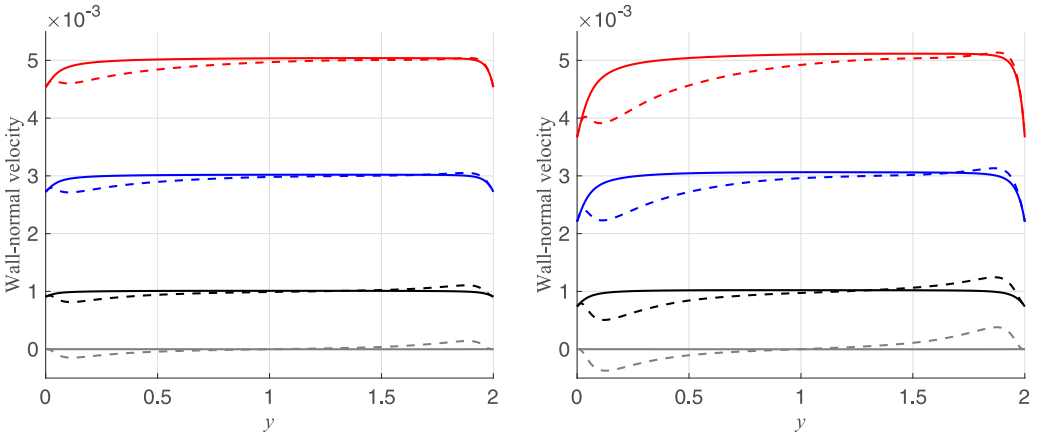

FIG. 17. Favre-averaged (solid lines) and Reynolds-averaged (dashed lines) wall-normal velocity for Ma = 0.8 (left) and Ma = 1.5 (right) for the uncontrolled case (gray), 0.1% (black), 0.3% (blue), and 0.5% (red).

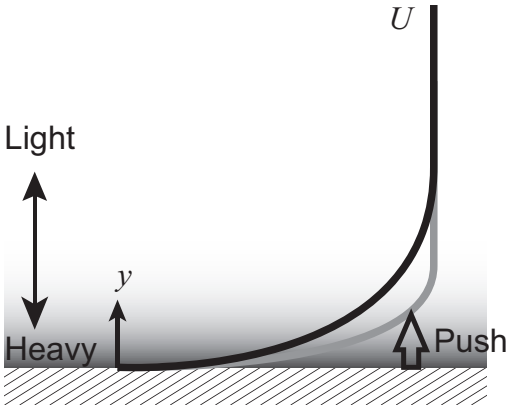

FIG. 18. Effect of Mach number on drag reduction by blowing.

caused by

$$\begin{aligned}\{v\} - \langle v\rangle &= \frac{\langle \rho v\rangle}{\langle \rho\rangle} - \langle v\rangle \\ &= \frac{\langle\langle \rho\rangle\langle v\rangle + \rho' v'\rangle}{\langle \rho\rangle} - \langle v\rangle \\ &= \langle v\rangle + \frac{\langle \rho' v'\rangle}{\langle \rho\rangle} - \langle v\rangle \\ &= \frac{\langle \rho' v'\rangle}{\langle \rho\rangle}. \end{aligned} \tag{22}$$

Here $\langle\rho\rangle$ is positive throughout the channel, so the correlation between the fluctuations of the density and the wall-normal velocity determine the gap between the Favre- and the Reynolds-averaged wall-normal velocities. Figure 18 shows the schematic of the streamwise mean velocity influenced by blowing. Near the lower wall, the positive wall-normal velocity fluctuation v' carries heavy fluid to a region with lighter fluid as shown in Fig. 18 and the positive fluctuation is induced (see Fig. 7). Hence, a positive correlation $\rho' v'$ is obtained. Similarly, from the upper wall, a negative v' will induce also the positive ρ' so that the negative $\rho' v'$ is obtained. As stated in Eq. (22), the difference between the Favre-averaged and the Reynolds-averaged v is $\langle \rho' v'\rangle/\langle\rho\rangle$, where $\langle\rho\rangle > 0$. Near the lower wall, since $\langle \rho' v'\rangle/\langle\rho\rangle$ is positive, then $\{v\} > \langle v\rangle$. On the other hand, near the upper wall, since $|\langle \rho' v'\rangle|$ decreases, $\{v\}$ approaches $\langle v\rangle$ as depicted in Fig. 19. As a result, the difference between the Reynolds-averaged and the Favre-averaged wall-normal velocities diminishes on the suction side.

As shown in Fig. 16, the net-energy saving rate S tends to be determined by the amplitude of the blowing mass flux because the wall-normal gradient of the streamwise velocity is more moderate with the stronger blowing. A similar mechanism was mentioned by Kametani and Fukagata [18] for the incompressible turbulent boundary layer. The Mach-number dependence of the control gain G is supposed to be caused by the increased density near the wall. Since the control input W_{in} is proportional to $\langle v_w\rangle^3$, W_{in} decreases as the bulk Mach number increases under the condition of constant blowing mass flux. Although the wall-normal momentum flux is constant, the wall-normal velocity on the blowing side is decreased since the density is increased near the wall as shown in Fig. 17. As the Mach number increases, the density near the wall is increased, so the control input W_{in} becomes smaller. As shown in Fig. 18, by blowing, the mean streamwise velocity profile shifts toward the channel center with reduction of the wall shear stress. As the Mach number increases, the control input power is decreased because of the increased density near the wall. In order to push

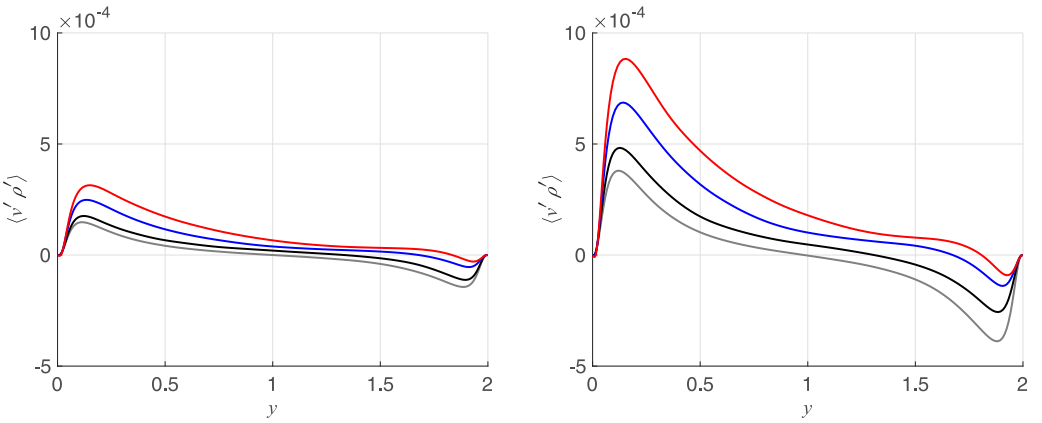

FIG. 19. Correlation of density and wall-normal velocity fluctuation $\langle \rho' v' \rangle$ for Ma = 0.8 (left) and Ma = 1.5 (right) for the uncontrolled case (gray), 0.1% (black), 0.3% (blue), and 0.5% (red).

up heavier fluids, more blowing velocity is required. The decreased blowing velocity input result in an increase of the control gain. On the other hand, the Mach-number dependence of the net-energy saving rate is less clear because the control input W_{in} is negligibly small.

Here the readers might have a concern about the effect of blowing with adiabatic walls because most cases of external flow assume the adiabatic walls. In contrast to the isothermal walls, the density is decreased and temperature is increased on adiabatic walls (see, e.g., Ref. [34]). The drag reduction effect by uniform blowing on an adiabatic wall should be basically similar to that on the isothermal wall because the third term of the FIK identity (C^{BS}) is the main contributor to the drag reduction effect. Concerning the net-energy saving rate, however, the input power of blowing is predicted to be increased due to reduced density on the wall.

E. Decomposition of the skin friction drag

Based on the compressible flow version of the FIK identity derived by Gomez *et al.* [27], the physical decomposition of the total friction drag in the presence of blowing and suction can be expressed as

$$
\begin{aligned}
C_f^{\text{FIK}} = \frac{2\tau_w^*}{\rho_b^* U_b^{*2}} &= C^L + C^T + C^{\text{BS}} + C^\mu + C^{\mu T} \\
&= \underbrace{\frac{6}{\text{Re}}}_{C^L} + \underbrace{3\int_0^2 (1-y)\langle\rho\rangle\{-u''v''\}dy}_{C^T} + \underbrace{3\int_0^2 (1-y)\langle\rho\rangle(-\{u\}\{v\})dy}_{C^{\text{BS}}} \\
&\quad + \underbrace{\frac{6}{\text{Re}}\int_0^2 (1-y)(\langle\mu\rangle - 1)\frac{\partial\langle u\rangle}{\partial y}dy}_{C^\mu} + \underbrace{\frac{6}{\text{Re}}\int_0^2 (1-y)\left\langle\mu'\left(\frac{\partial u'}{\partial y} + \frac{\partial v'}{\partial x}\right)\right\rangle dy}_{C^{\mu T}}, \quad (23)
\end{aligned}
$$

which decomposes the skin friction drag into four components, i.e., contributions from the laminar flow, the Reynolds shear stress, blowing and suction, the compressible contribution, and the compressible-turbulent interaction. In the incompressible case, the corresponding components are C^L, C^T, and C^{BS} (see Ref. [17]). The decomposed total skin friction drag is depicted in Fig. 20. Here the total skin friction, i.e., the average of the friction coefficient of the blowing and suction sides, is discussed. Because of the different friction Reynolds numbers, the total values are not comparable. The balance of all the components is shown in Table IV. Since the bulk Reynolds

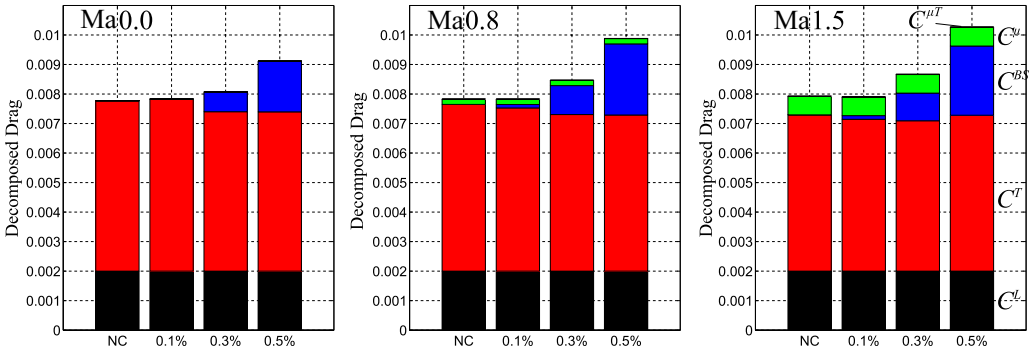

FIG. 20. Decomposed skin friction drag for C^L (black), C^T (red), C^{BS} (blue), C^μ (green), and $C^{\mu T}$ [gray (invisible)].

number is fixed, C^L is constant in all cases. The dominant contributors are C^L, C^T, C^{BS}, and C^μ. The compressible-turbulent interaction term $C^{\mu T}$ is negligibly small. The Reynolds shear stress term C^T tends to decrease by the blowing and suction in all bulk-Mach-number cases due to the following two reasons: (i) Turbulence is shifted away from the wall on the blowing side and (ii) turbulence is decreased on the suction side. It should be noticed that, in the Ma1.5 case, C^T is increased again from a 0.3% to a 0.5% blowing-suction amplitude because the enhancement of RSS by blowing overcomes the reduction of RSS by suction. At the same bulk Reynolds number, C^T in Ma0.8 is larger than that in Ma1.5 for all blowing amplitudes including uncontrolled case, while C^μ in Ma0.8 is smaller than that in Ma1.5.

Unlike the Reynolds shear stress term C^T, the blowing and suction term C^{BS} is negligibly small at all Mach numbers at 0.1% of blowing and suction. For 0.3% blowing and suction cases, C^{BS} increases up to around eight times larger than that of the 0.1% blowing and suction cases at all Mach numbers.

The compressible contribution term C^μ appears only in the compressible cases. The amount of C^μ increases as the Mach number increases, while it is hardly affected by the control amplitude. The integrand of C^μ in Eq. (23) is very small near the wall because the viscosity on the wall is unity, i.e., $\lim_{y\to 0}(\langle\mu\rangle - 1) = 0$. This is a consequence of the constant wall temperature condition. On the other hand, with an increase of Mach number, C^μ increases due to the increased viscosity in the vicinity of the wall.

TABLE IV. Different contribution of the FIK identity ($\times 10^3$).

Case	C^L	C^T	C^{BS}	C^μ	$C^{\mu T}$	Total
Ma0.0	2.0	5.77	0.00			7.78
Ma0.0BS0.1	2.0	5.83	$O(10^{-3})$			7.83
Ma0.0BS0.3	2.0	5.40	0.67			8.07
Ma0.0BS0.5	2.0	5.39	1.72			9.11
Ma0.8	2.0	5.65	0.00	0.18	$O(10^{-3})$	7.83
Ma0.8BS0.1	2.0	5.20	0.12	0.18	$O(10^{-3})$	7.90
Ma0.8BS0.3	2.0	5.30	0.98	0.18	$O(10^{-3})$	8.47
Ma0.8BS0.5	2.0	5.49	2.00	0.18	$O(10^{-3})$	9.68
Ma1.5	2.0	5.30	0.00	0.62	0.02	7.93
Ma1.5BS0.1	2.0	5.14	0.12	0.62	0.02	7.91
Ma1.5BS0.3	2.0	5.09	0.94	0.63	0.01	8.67
Ma1.5BS0.5	2.0	5.28	2.34	0.64	0.01	10.3

V. SUMMARY AND CONCLUSIONS

A series of DNSs of compressible turbulent channel flows with uniform blowing and suction were performed in order to investigate the Mach-number effect of uniform blowing and suction from the wall. Similarly to the incompressible turbulent channel flow, drag reduction on the blowing side and drag increase on the suction side were confirmed.

The present DNS results show that the drag reduction rate is primarily affected by the control amplitude rather than the bulk Mach number. A similar trend appears on the net-energy saving rate because of the small amplitude of blowing. In contrast, the control gain has a clear Mach-number dependence: It increases as the bulk Mach number increases. This was explained by the decrease of wall-normal velocity due to the increased density near the wall. The decomposition of the skin friction drag using the FIK identity confirms the absence of the Mach number dependence except for the viscosity term C^{μ}, which comes from the viscosity variation due to temperature.

In summary, the Mach-number dependence on the uniform blowing and suction effect in a supersonic turbulent channel flow is merely due to the varied thermal properties such as density and temperature, similarly to the Mach-number dependence on the turbulent statistics in uncontrolled flows. This in turn suggests that the uniform blowing, which has been extensively studied for drag reduction of incompressible flows, can effectively be used also for supersonic turbulent boundary layers.

ACKNOWLEDGMENTS

The authors are grateful to Dr. Shinnosuke Obi and Dr. Keita Ando (Keio University) for fruitful discussion. This work was done in the framework of Silent Supersonic Aircraft Research Program of Japan Aerospace Exploration Agency and partly supported through the Japan Society for the Promotion of Science (Japan), KAKENHI Grant No. JP16K06900.

[1] J. Jiménez, Near-wall turbulence, Phys. Fluids **25**, 101302 (2013).
[2] J. Kim, P. Moin, and R. Moser, Turbulence statistics in fully developed channel flow at low Reynolds number, J. Fluid Mech. **177**, 133 (1987).
[3] J. Kim, Control of turbulent boundary layers, Phys. Fluids **15**, 1093 (2003).
[4] R. Garcia-Mayoral and J. Jiménez, Drag reduction by riblets, Philos. Trans. R. Soc. A **369**, 1412 (2011).
[5] J. P. Rothstein, Slip on superhydrophobic surfaces, Annu. Rev. Fluid Mech. **42**, 89 (2010).
[6] S. Türk, G. Daschiel, A. Stroh, Y. Hasegawa, and B. Frohnapfel, Turbulent flow over superhydrophobic surfaces with streamwise grooves, J. Fluid Mech. **747**, 186 (2014).
[7] J. Kim and T. R. Bewley, A linear systems approach to flow control, Annu. Rev. Fluid Mech. **39**, 383 (2007).
[8] N. Kasagi, Y. Suzuki, and K. Fukagata, Microelectromechanical system-based feedback control of turbulence for skin friction reduction, Annu. Rev. Fluid Mech. **41**, 231 (2009).
[9] H. Choi, P. Moin, and J. Kim, Active turbulence control for drag reduction in wall bounded flows, J. Fluid Mech. **262**, 75 (1994).
[10] T. Min, S. M. Kang, and J. L. Speyer, Sustained sub-laminar drag in a fully developed channel flow, J. Fluid Mech. **558**, 309 (2006).
[11] T. R. Bewley, A fundamental limit on the balance of power in a transpiration-controlled channel flow, J. Fluid Mech. **632**, 443 (2009).
[12] K. Fukagata, K. Sugiyama, and N. Kasagi, On the lower bound of net driving power in controlled duct flows, Physica D **238**, 1082 (2009).
[13] R. Nakanishi, H. Mamori, and K. Fukagata, Relaminarization of turbulent channel flow using traveling wave-like wall deformation, Int. J. Heat Fluid Flow **35**, 152 (2012).

[14] H. Mamori, K. Iwamoto, and A. Murata, Effect of the parameters of traveling waves created by blowing and suction on the relaminarization phenomena in fully developed turbulent channel flow, Phys. Fluids **26**, 015101 (2014).
[15] T. N. Stevenson, A law of the wall for turbulent boundary layers with suction or injection, College of Aeronautics (Cranfield) Report No. 166 1963 (unpublished).
[16] Y. Sumitani and N. Kasagi, Direct numerical simulation of turbulent transport with uniform wall injection and suction, AIAA J. **33**, 1220 (1995).
[17] K. Fukagata, K. Iwamoto, and N. Kasagi, Contribution of the Reynolds stress distribution to the skin friction in wall bounded flows, Phys. Fluids **14**, L73 (2002).
[18] Y. Kametani and K. Fukagata, Direct numerical simulation of spatially developing turbulent boundary layers with uniform blowing or suction, J. Fluid Mech. **681**, 154 (2011).
[19] Y. Kametani, K. Fukagata, R. Örlü, and P. Schlatter, Effect of uniform blowing/suction in a turbulent boundary layer at moderate Reynolds number, Int. J. Heat Fluid Flow **55**, 132 (2015).
[20] Y. Kametani, K. Fukagata, R. Örlü, and P. Schlatter, Drag reduction in spatially developing turbulent boundary layers by spatially intermittent blowing at constant mass-flux, J. Turbul. **17**, 913 (2016).
[21] D. Noguchi, K. Fukagata, and N. Tokugawa, Friction drag reduction of a spatially developing boundary layer using a combined uniform suction and blowing, J. Fluid Sci. Technol. **11**, JFST0004 (2016).
[22] K. Ushiyama, H. Ishikawa, N. Tokugawa, and K. Koike, Natural laminar flow wing design for a small supersonic transport QSST (in Japanese), JAXA Research and Development Report No. JAXA-RR-16-001, 2016, https://repository.exst.jaxa.jp/dspace/handle/a-is/576007?locale=en.
[23] G. N. Coleman, J. Kim, and R. D. Moser, A numerical study of turbulent supersonic isothermal-wall channel flow, J. Fluid Mech. **305**, 159 (1995).
[24] Y. Morinishi, S. Tamano, and K. Nakabayashi, Direct numerical simulation of compressible turbulent channel flow between adiabatic and isothermal walls, J. Fluid Mech. **502**, 273 (2004).
[25] H. Foysi, S. Sarkar, and R. Friedrich, Compressibility effects and turbulence scaling in supersonic channel flow, J. Fluid Mech. **509**, 207 (2004).
[26] M. Lagha, J. Kim, J. Eldredge, and X. Zhong, A numerical study of compressible turbulent boundary layers, Phys. Fluids **23**, 015106 (2011).
[27] T. Gomez, V. Flutet, and P. Sagaut, Contribution of Reynolds stress distribution to the skin friction in compressible turbulent channel flows, Phys. Rev. E **79**, 035301 (2009).
[28] K. Fukagata, N. Kasagi, and P. Koumoutsakos, A theoretical prediction of friction drag reduction in turbulent flow by superhydrophobic surfaces, Phys. Fluids **18**, 051703 (2006).
[29] Y. Morinishi, T. S. Lund, O. V. Vasilyev, and P. Moin, Fully conservative higher order finite difference schemes for incompressible flow, J. Comput. Phys. **143**, 90 (1998).
[30] P. R. Spalart, R. D. Moser, and M. M. Rogers, Spectral methods for the Navier-Stokes equations with one infinite and two periodic directions, J. Comput. Phys. **96**, 297 (1991).
[31] F. E. Ham, F. S. Lien, and A. B. Strong, A fully conservative second-order finite difference scheme for incompressible flow on non-uniform grids, J. Comput. Phys. **177**, 117 (2002).
[32] A. A. Amsden and F. H. Harlow, A simplified MAC technique for incompressible fluid flow calculations, J. Comput. Phys. **6**, 322 (1970).
[33] P. G. Huang, G. N. Coleman, and P. Bradshaw, Compressible turbulent channel flows DNS results and modeling, J. Fluid Mech. **305**, 185 (1995).
[34] S. Tamano and Y. Morinishi, Effect of different thermal wall boundary conditions on compressible turbulent channel flow at $M = 1.5$, J. Fluid Mech. **548**, 361 (2006).